Fabrication and characterization of $ZnGa_{1.01}Te_{2.13}$/g-C_3N_4 heterojunction with enhanced photocatalytic activity

Chiing-Chang Chen [a,1], Wen-Jin Liu [a,1], Janah Shaya [b,c], Yu-Yun Lin [a], Fu-Yu Liu [a], Chao-Wei Chen [a], Hwei-yan Tsai [d,e], Chung-Shin Lu [f,*]

[a] *Department of Science Education and Application, National Taichung University of Education, Taichung 403, Taiwan*
[b] *Department of Chemistry, Khalifa University of Science and Technology, Abu Dhabi 127788, United Arab Emirates*
[c] *Advanced Materials Chemistry Centre (AMCC), SAN Campus, Khalifa University, Abu Dhabi P.O. Box 127788, United Arab Emirates*
[d] *Department of Medical Applied Chemistry, Chung Shan Medical University, Taichung 402, Taiwan*
[e] *Department of Medical Education, Chung Shan Medical University Hospital, Taichung 402, Taiwan*
[f] *Department of General Education, National Taichung University of Science and Technology, Taichung 403, Taiwan*

ARTICLE INFO

ABSTRACT

The extensive consumption of fossil fuels increases CO_2 concentration in the atmosphere, resulting in serious global warming problems. Meanwhile, the problem of water contamination by organic substances is another significant global challenge. We have successfully synthesized $ZnGa_{1.01}Te_{2.13}$/g-C_3N_4 (ZGT/GCN) composites for the first time as effective photocatalysts for both pollutant degradation and CO_2 reduction. ZGT/GCN composites were synthesized by a simple hydrothermal method. The prepared photocatalysts were characterized by XRD, SEM, TEM-EDS, DRS, BET, PL, and XPS. The ZGT/GCN heterojunction exhibited considerably enhanced photocatalytic activity in the degradation of crystal violet (CV) as well as in the photoreduction of CO_2 when compared to pure ZGT and GCN semiconductors. The optimal rate constant for CV degradation was obtained with the ZGT-80%GCN composite ($0.0442 \ h^{-1}$), which is higher than the constants obtained with individual ZGT and GCN by 7.75 and 1.63 times, respectively. Moreover, the CO_2 reduction yields into CH_4 by ZGT-80%GCN was 1.013 μmol/g in 72 h, which is 1.21 and 1.08 times larger than the yields obtained with ZGT and GCN. Scavenger and ESR tests were used to propose the photocatalytic mechanism of the ZGT/GCN composite as well as the active species in the CV degradation.

1. Introduction

The excessive use of fossil fuels in modern life has led to dramatic increase in the concentration of CO_2 in the atmosphere, raising serious environmental concerns such as global warming, melting of glaciers, and rise of sea levels [1–4]. Several approaches are investigated to mitigate the environmental impact of CO_2, among which chemical conversion of CO_2 into fuel molecules or value-added products can additionally serve in alleviating the present scenario of energy shortage [5]. Organic pollutants, such as widely used dyes and pigments, represent another environmental pollution problem in industrial wastewater discharges, with many

---

contaminants being non-biodegradable and potentially carcinogenic [6]. In particular, triphenylmethane dyes (e.g., Crystal Violet (CV)) are commonly used in several industries such as food, paper and cosmetics industries [7]. Wastewater containing triphenylmethane dyes is a considerable source of water pollution. These dyes majorly interfere with light penetration and alter the photosynthetic reactions in aquatic plants, impacting the aquatic ecosystem. Triphenylmethane dyes are also classified as carcinogenic and toxic chemicals, which pose serious risks to humans and aquatic organisms [8]. Heterogeneous photocatalysis has emerged as a promising technology for the two described environmental problems. This technology can be effective in degradation of pollutants into CO_2, H_2O, and other inorganic substances and additionally in useful chemical conversions of CO_2 into fuels, such as CH_3OH, CH_4, and CO. Photocatalysis has gained significant attention in these processes for its high efficiency and low cost as well as for the utilization of solar energy as the main energy source [6,9–11].

To find suitable photocatalysts for CO_2 reduction, Singh et al. [12] used 6 screening criteria to evaluate the synthesizability, visible-light absorption, electronic structure, energy gap, and corrosion resistance of 68,860 inorganic compounds. Some materials in the screening process, such as $ZnGa_2X_4$ (X = Se, Te), were found to meet all the requirements for photoreduction of CO_2 although their photocatalytic properties have not been reported yet. Inspired by Singh's work, we set up to synthesize the Zn-Ga-Te (ZGT) materials in order to investigate their photocatalytic activity for CO_2 reduction and dye degradation.

Ternary zinc digallium telluride ($ZnGa_2Te_4$) materials belong to the group of defect chalcopyrite tetragonal $II–III_2–VI_4$ semiconductors. These materials are characterized by their remarkable characteristics such as bright photoluminescence, wide bandgap, high photosensitivity and stability of several parameters [13]. These properties attracted considerable research focusing on this ternary group for their prospective applications in memory and nonlinear optical devices, solar cells, ultra-violet photodetectors, narrow-band optical filters, and Schottky diodes [14–17]. On the other hand, graphitic carbon nitride ($g-C_3N_4$, GCN) materials have gained similar research interest for their beneficial properties such as stability, nontoxicity, strong visible-light absorption, narrow bandgap (2.7 eV), and favorable electrical properties [7,18–23]. The ease of synthesis of GCN subsequently favors their applications. GCN can be easily produced by thermal condensation of common nitrogen-rich reagents such as melamine and urea [24]. GCN-based materials are investigated for their prospective photocatalytic applications such as reduction of CO_2, decomposition of organic contaminants, and water splitting [25–29]. Recently, Sb_2MoO_6/GCN, $ZnCo_2O_4$/GCN, $Ag_2C_2O_4$/Ag/GCN, VO_x/GCN, and Bi7O9I3/GCN composites have been reported with enhanced photocatalytic performance attributed to the role of the GCN in better separation of the charge carriers responsible for catalytic activity [30–34].

In this work, we report the synthesis of ZGT/GCN composites ($ZnGa_{1.01}Te_{2.13}$/$g-C_3N_4$) via a simple hydrothermal process, their characterization (XRD, HRTEM, SEM-EDS, BET, DRS, and XPS), and efficient photocatalytic applications. The ZGT/GCN materials showed significant improvement in both photocatalytic reduction of CO_2 and degradation of CV dye as compared to pristine ZGT and GCN. Furthermore, the ZGT/GCN photocatalysts showed good chemical stability and durability in several photocatalysis recycling experiments. This work also presents the proposed photocatalytic degradation mechanism of CV and the active species entailed in the process based on scavenger and ESR experiments.

2. Experimental

2.1. Materials

The reagents were purchased from the following suppliers and used without further purification: zinc nitrate hexahydrate, gallium *nitrate*, sodium azide and 5,5-Dimethyl-1-pyrroline *N*-oxide (DMPO) from Sigma-Aldrich; tellurium powder, melamine and *p*-benzoquinone from Alfa Assar; 1-(2-aminoethyl)piperazine (AEP) from Acros Organics; CV dye from TCI; ammonium oxalate from Shimakyu Chemical; reagent-grade HNO_3, sodium hydroxide, ammonium acetate, HPLC-grade isopropanol and methanol from Merck. Deionized water was used in all experiments after purification using a Milli-Q water ion exchange system to obtain a resistivity of 1.8×10^7 Ω-cm.

2.2. Apparatus and instruments

X-ray powder diffraction (XRD) was investigated using a MAC Science MXP18 equipped with Cu-Ka radiation, operated at 40 kV and 80 mA. JEOL JSM-7401F instrument (accelerating voltage = 15 kV) was used for field-emission scanning electron microscopy-electron dispersive X-ray spectroscopy (FE-SEM-EDS). High-resolution transmission electron microscopy (HRTEM) images, energy-dispersive X-ray spectra (EDS), and selected area electron diffraction (SAED) patterns were studied using a JEOL-2010 instrument (accelerating voltage = 200 kV). Photoluminescence (PL) measurements were performed using Hitachi F-7000 instrument, high-resolution X-ray photoelectron spectroscopy (HRXPS) using ULVAC-PHI instrument, and ultra-violet photoelectron spectroscopy (UPS) using ULVAC-PHI XPS, PHI Quantera SXM. Photocurrent and electrochemical impedance spectroscopy (EIS) were conducted using an electrochemical analyzer from CH Instrument Company. A standard three-electrode configuration system was used with a Pt wire serving as the counter electrode and a calomel electrode used as the reference electrode. A Micrometrics Gemini automated system with N_2 gas (adsorbate) at liquid nitrogen temperature was utilized to determine the Brunauer-Emmett-Teller (BET) specific surface areas. The electron spin resonance (ESR) signals of $^\bullet O_2^-$ and $^\bullet OH$ radical species, trapped using DMPO, were recorded using a Bruker EMX A300-10/12 with a microwave bridge (modulation frequency, 100 kHz; modulation amplitude, 1 G; microwave power, 22.8 mW; microwave frequency, 9.85 GHz).

2.3. Synthesis of ZGT/GCN

For the preparation of the ZGT catalyst, 0.25 mmol of zinc nitrate hexahydrate ($Zn(NO_3)_3 \bullet 6H_2O$), 1.0 mmol of gallium *nitrate* ($Ga(NO_3)_3 \bullet xH_2O$), 2.24 mmol of tellurium powder, and 19.35 mmol of N-(2-aminoethyl)piperazine (AEP) were mixed in water (3.0 g, 166.7 mmol) and stirred for 1 h. The slurry was next transferred into a 23-mL Teflon-lined stainless-steel autoclave and heated for 9 days at 200 °C. The reaction mixture was left to cool down to room temperature. The obtained precipitate was filtered, washed with absolute ethanol and deionized water several times, and dried overnight at 60 °C.

The synthesis of the GCN was performed via melamine calcination under atmospheric conditions in a muffle furnace. First, 5 g of melamine was heated at a rate of 10 °C/min to a final temperature of 540 °C (4 h) in an alumina crucible. After cooling to room temperature, the powder was grinded in an agate mortar to obtain graphitized carbon nitride (GCN). The typical preparation of ZGT/ GCN composites was as follows: an appropriate amount of GCN was dispersed in ethylene glycol (10 mL) by ultrasonication. The as-prepared ZGT powder was subsequently transferred into the GCN solution followed by stirring for 30 min at rt. The mixture was then placed in a 23 mL Teflon-lined autoclave and heated to 100 °C for 4 h. The solid precipitate was filtered, washed with deionized water, and dried overnight (60 °C). The ZGT/GCN samples with varied weight ratios of GCN (5 %, 10 %, 20 %, 30 %, 40 %, 50 %, 60 %, 70 %, 80 %, and 90 %, respectively) were synthesized according to the method as mentioned above. All samples are presented as ZGT-*x*% GCN; *x* represents the weight content of GCN.

2.4. Photocatalytic experiments

2.4.1. Photocatalytic degradation of CV

Photocatalytic degradation of CV dye was used to assess the photocatalytic activity of ZGT/GCN composites under visible-light irradiation. The irradiation was conducted using a 15 W fluorescent lamp, and the reaction vessel was positioned 30 cm away from the light source. The lamp predominantly emits visible light within the range of 400–700 nm A typical photocatalytic run consisted of a 100 mL aqueous suspension of CV dye (10 ppm) and 10 mg of the photocatalyst in a Pyrex reaction vessel. The pH of the suspension was adjusted using nitric acid or sodium hydroxide solution as required in each experiment. Prior to irradiation, the suspension was stirred in the dark for ~30 min to establish the adsorption/desorption equilibrium. Aliquots (5 mL each) were collected at certain irradiation time intervals. The photocatalyst was removed from the aliquot by centrifugation. The supernatant was then measured using UV-PDA, and residual CV dye was determined at a wavelength of 580 nm.

2.4.2. Photocatalytic reduction of CO_2

A compressed steel cylinder containing carbon dioxide (99.99 %) was adjusted by the mass flow controller at a delivery rate of 20 mL/min. The reactor was previously checked for leaks for several hours under a pressure of 2 bar and purged with He gas. The process of CO_2 saturation was carried out in a photoreactor containing 0.1 g of the photocatalyst in an aqueous NaOH solution (1 N). The samples after the photoreduction were obtained from the photoreactor using a gas-tight syringe. The analysis of the CO_2 content and the photoreduction products was carried out by 1 mL injections of gas samples into Thermo Trace 1300 gas chromatography (GC) instrument, equipped with a flame ionization detector (FID) and thermal conductivity detector (TCD). The FID detector was connected to a TG-BOND-Q column (30 m length, 0.32 mm ID, 10 μm film) for the separation of alcohols, hydrocarbons and other oxygenated products. The TCD detector was connected to a TG-BOND MSieve 5A column (30 m length, 0.32 mm ID, 30 μm film) for the separation of light gases (CO_2, CO, O_2, N_2 and H_2). The carrier gases used were N_2 (99.9995 %) or He (99.999 %). The quantitative calibration curve was obtained using high-purity standard gases (CO, CO_2, CH_4, C_2H_6, H_2) and ~5000 ppm of various mixed gases (CO_2, CO, CH_4, H_2, etc.) in the GC system. Table S1 (Supplementary Material) presents the details of the adopted procedure. Fig. S1 shows the calibration curves of the different gases (CO_2, CO, CH_4, CH_3OH, C_2H_5OH, HCOOH, and H_2). The GC chromatogram of the gas mixture comprising CO_2, CO, CH_4, CH_3OH, C_2H_5OH and HCOOH shows favorable separation. The procedure described by the US
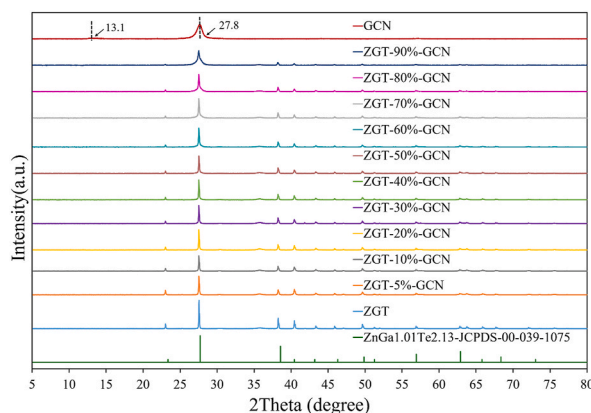

Fig. 1. XRD patterns of the as-prepared ZGT/GCN samples with different mass ratios of GCN.

Environmental Protection Agency was used for the method detection limit (MDL) of the GC system. The respective MDLs of CO_2, CO, CH_4, CH_3OH, C_2H_5OH, HCOOH and H_2 were 3.21, 2.43, 2.13, 8.13, 4.68, 31.68 and 23.0 ppm.

3. Results and discussion

3.1. Characterization of ZGT/GCN composites

3.1.1. Phase structure

The XRD patterns of the pure ZGT, GCN, and the ZGT/GCN composites with various mass ratios of GCN are displayed in Fig. 1. The GCN sample is characterized by the peak located at 27.8° arising from the interlayer stacking of aromatic groups and that at 13.1° corresponding to an in-plane structural packing [35]. The pristine ZGT sample shows diffraction peaks that correspond to the $ZnGa_{1.01}Te_{2.13}$ phase (JCPDS-00-039-1075). The main peaks can be indexed as (4 0 0), (3 2 2), (2 1 4), (3 0 4), (7 3 1), (4 4 4), (2 0 6), (10 2 1), (2 2 7) and (10 1 4) planes of tetragonal $ZnGa_{1.01}Te_{2.13}$ (Fig. S2). Moreover, the ZGT/GCN composites display XRD patterns of both GCN and ZGT. The diffraction peaks of GCN become weaker with the increase of ZGT content, which suggest the coexistence of GCN and ZGT in ZGT/GCN samples. The absence of other impurity peaks indicates that the as-synthesized ZGT/GCN composites are pure and stable.

The Fourier transform infrared spectra (FTIR) of the ZGT, GCN, and ZGT-80%GCN were recorded (Fig. S3). The characteristic absorption peaks of graphitic carbon nitride are displayed in both the pure GCN and the ZGT-80%GCN. The characteristic breathing mode of s-triazine can be seen at 810 cm^{-1}. The peaks in the 1200–1650 cm^{-1} range are attributed to the stretching mode of the C–N heterocycles, and the broad ones in the 2800–3400 cm^{-1} range are ascribed to the primary and secondary amines of the aromatic groups [36]. In addition to GCN peaks, the peaks belonging to ZGT are found in the ZGT-80%GCN, confirming the formation of the heterojunction in agreement with the XRD results.
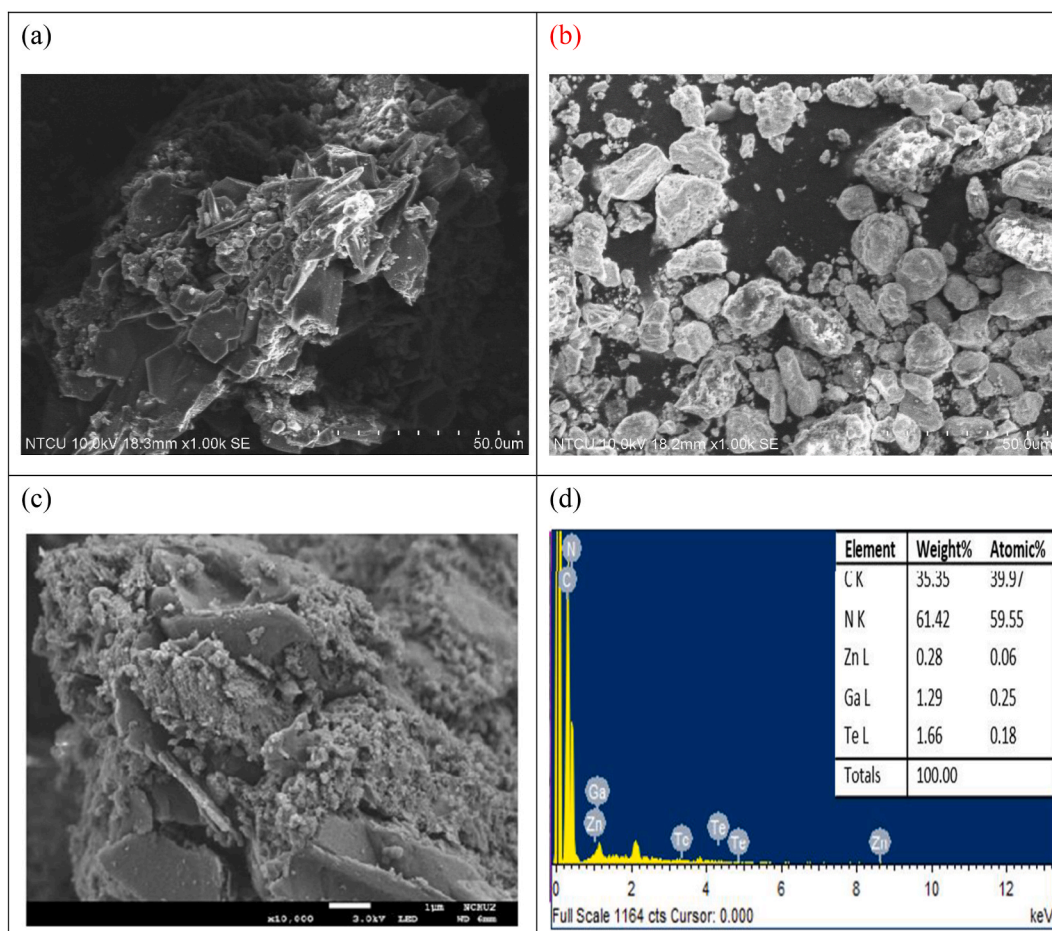

Fig. 2. FE-SEM of the as-prepared (a) GCN, (b) ZGT, (c) ZGT-80%GCN and (d) EDS of the ZGT-80%GCN.

3.1.2. Morphological structure and composition

The surface morphologies of the ZGT/GCN composites were examined by FE-SEM-EDS. The pure GCN sample displays a layered structure with many stacking layers (Fig. 2a), as previously described in the literature [37]. Fig. 2b depicts the SEM image of pristine ZGT powder, showing its morphology as clusters of aggregates of smaller particles formed in irregular stack shapes. Fig. 2c shows the deposition of the ZGT on the surface of GCN and the formation of the composite structure. The EDS result (Fig. 2d) demonstrates that zinc, gallium, tellurium, carbon and nitrogen are the major elements within these composites. Fig. 3 depicts the FE-TEM-EDS images of ZGT-80%GCN sample, revealing the interfacial interaction between ZGT and GCN. The lattice spacing of 0.273 nm associated to the (10 1 4) crystal plane of $ZnGa_{1.01}Te_{2.13}$ is in close contact to the 0.326 nm spacing relevant to the (0 0 2) GCN crystal plane [38]. These results affirm the coexistence of $ZnGa_{1.01}Te_{2.13}$ and GCN in the prepared materials, in agreement with the XRD characterization.

3.1.3. X-ray photoelectron spectroscopy

The ZGT-80%GCN sample was analyzed by XPS to confirm the surface chemical composition and the valence state of elements. Two symmetric peaks were observed at 1021.8 and 1044.9 eV in Fig. 4a, characteristic of the spin-orbit split of Zn 2p, indicating Zn $2p_{3/2}$ and Zn $2p_{1/2}$ signals induced by Zn^{2+} ions [39]. Ga 2p spectrum (Fig. 4b) shows Ga $2p_{3/2}$ and Ga $2p_{1/2}$ peaks for Ga^{3+} ions at 1117.9 and 1144.8 eV, respectively [40]. The Te spectrum (Fig. 4c) displays the $3d_{5/2}$ and $3d_{3/2}$ transitions by two respective signals at 572.6 and 583.0 eV and additional two peaks at 575.8 and 586.2 eV corresponding to $3d_{5/2}$ and $3d_{3/2}$ transitions from Te–O (the oxide phase of Te) [41]. The observed splitting in the N-1s spectrum (Fig. 4d) into three peaks (398.3, 400.2, and 404.0 eV) is attributed to C–N≡C (sp^2-N in triazine rings), N-(C)$_3$ (tertiary N), and lastly to the charging effects in the heterocycles [42,43]. The C-1s spectrum (Fig. 4e) exhibits the characteristic peak of sp^2-carbon in the GCN (N–C≡N) at 287.7 eV and an additional one at 284.6 eV from external hydrocarbon in the apparatus [44,45]. These results affirm the existence of GCN in the as-synthesized composites.
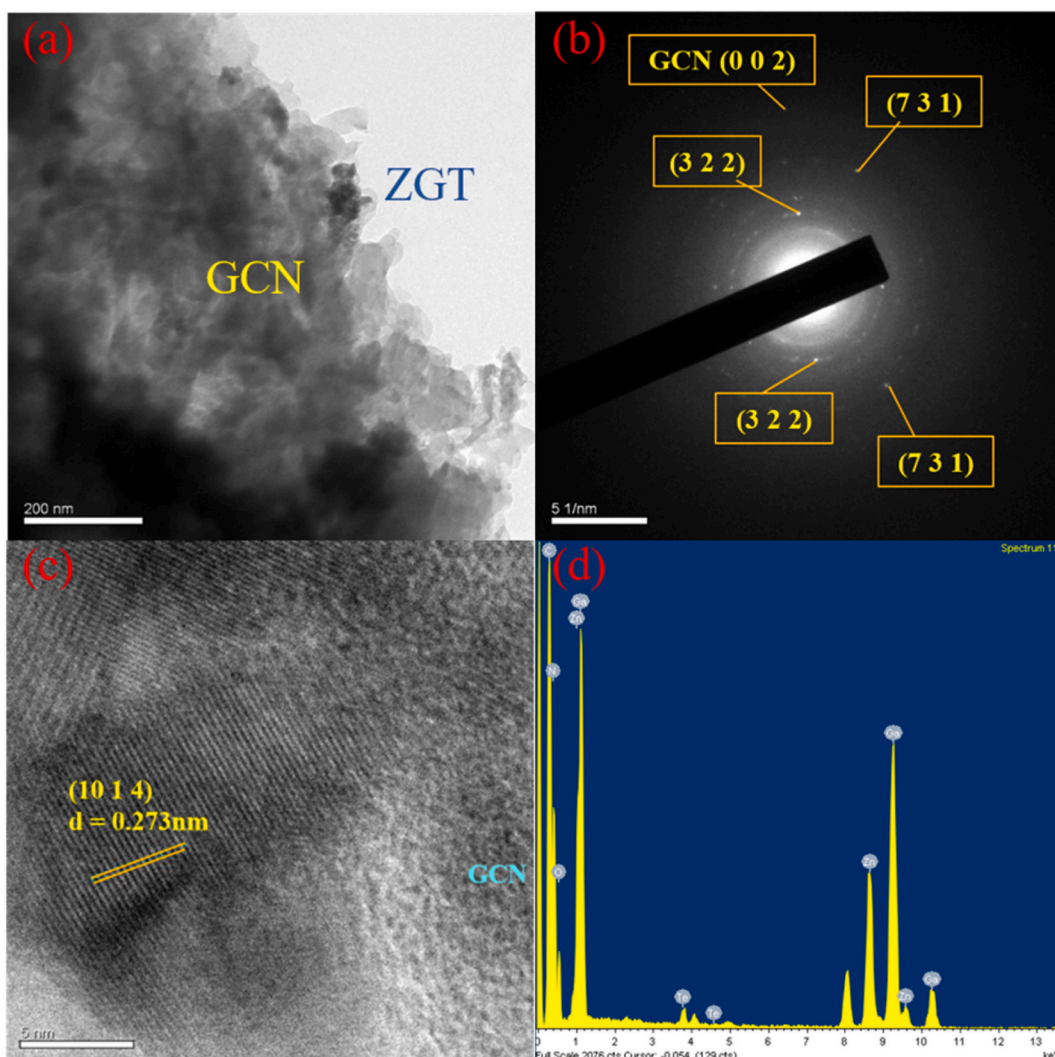

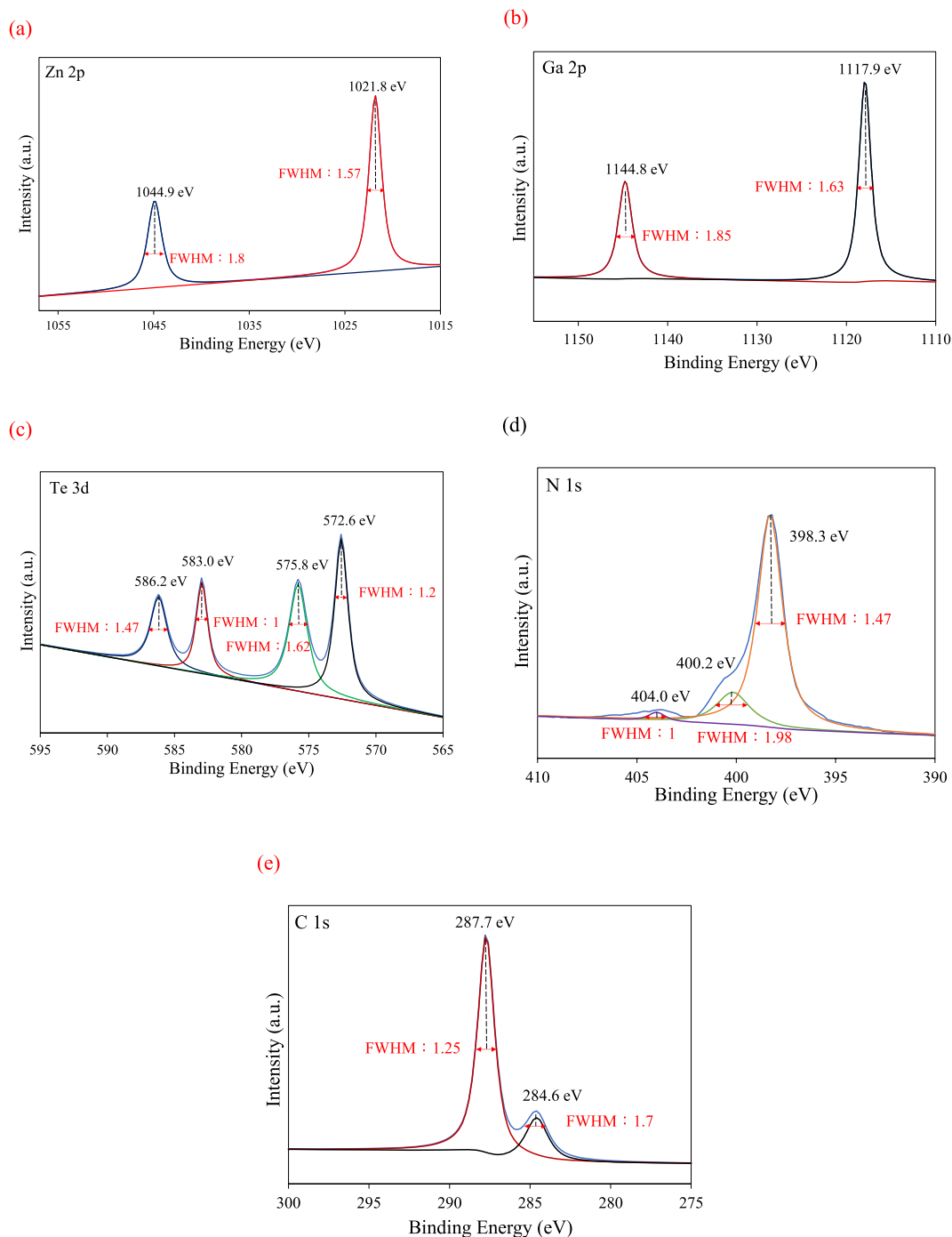**Fig. 3.** FE-TEM and EDS of the as-prepared ZGT-80%GCN composite.

(a)

(b)

(c)

(d)

(e)

Fig. 4. High resolution XPS spectra of the ZGT-80%GCN composite: (a) Zn 2p, (b) Ga 2p, (c) Te 3d, (d) N 1s, and (e) C 1s.

3.1.4. Optical absorption properties

The UV–vis diffuse reflectance spectra (DRS) were recorded for pure GCN, ZGT, and ZGT-80%GCN composites to investigate the optical absorption properties (Fig. 5). Pure GCN shows an absorbance edge around 470 nm, ascribed to its intrinsic bandgap of about 2.6 eV [46]. The similarity in the absorption band between the ZGT-80%GCN and pure GCN spectra indicates the minimal impact of introducing ZGT into GCN on the optical properties. $(\alpha h\nu)^n = k(h\nu - Eg)$ was used for estimating the bandgap energies (α: absorption coefficient; $h\nu$: photonic energy; k: constant; Eg: absorption bandgap energy; and n = 1/2 or 2 for an indirect or direct bandgap semiconductor, respectively) [47]. The bandgap energies of ZGT, GCN and ZGT-80%GCN were found to be about 3.3, 2.6 and 2.7 eV, respectively. These results show the potential of the synthesized semiconductors in visible-light driven photocatalytic applications.
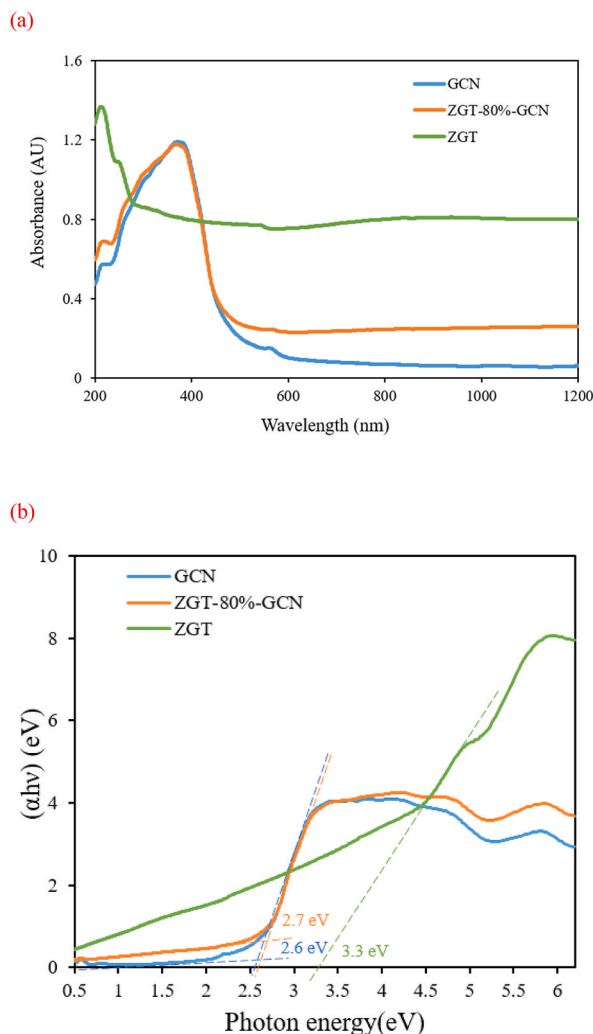
(a)

(b)

Fig. 5. DRS patterns of the as-prepared ZGT, GCN, and ZGT-80%GCN.

3.1.5. BET and adsorption-desorption isotherm

Fig. 6a-c presents the nitrogen adsorption-desorption isotherms and pore size distributions of the ZGT, GCN, and ZGT-80%GCN samples. Pristine GCN shows a type-III isotherm, which can be ascribed to either weak interaction between the adsorbate and adsorbent or the presence of adsorbed N_2 on the interlayer [48]. The ZGT-80%GCN photocatalyst exhibits type-III isotherm with a hysteresis loop close to Type H3 in the relative pressure range of 0.9–1.0 [49]. This type suggests the formation of slit-like pores by aggregation of plate-like particles [50]. The specific surface areas (S_{BET}), pore volumes, and average adsorption and desorption pore sizes of the samples are summarized in Table 1. S_{BET} of pristine ZGT, GCN, and ZGT-80%GCN were 19.1 m^2/g, 13.0 m^2/g, and 14.1 m^2/g, respectively. The BET surface area of the ZGT-80%GCN composite was larger than pure GCN. The smaller S_{BET} of ZGT-80%GCN than pristine ZGT might be due to the wrapping of some ZGT in the GCN that has a much larger particle size, reducing the surface area of ZGT-80%GCN after forming the composite [51].

3.2. Photocatalytic activity of ZGT/GCN composites

The visible-light photocatalytic activities of the different ZGT/GCN composites were investigated by photodegradation experiments of CV dye (Fig. 7). Among all samples, ZGT-80%GCN showed the best photocatalytic activity with 99 % of CV degradation after 96 h of irradiation with visible light (Fig. 7a). Fig. 7b shows the ln(Co/C) plots versus irradiation time (hr) used to investigate the kinetics and the rate constants (Table 2) of the photodegradation reactions with the different photocatalysts. The pseudo-first-order equation (ln(Co/C) = kt) was found to fit all the CV degradation over these catalysts [52]. The degradation rate constant over ZGT-80%GCN is 0.0442 h^{-1}; 7.75 and 1.63 times higher than the rate constants using pure ZGT or GCN, respectively. Table 3 presents a comparative analysis between the current study and other recently published research regarding the degradation of CV dye using various photocatalysts [7,38,53–58]. While some of the previous studies demonstrated favorable efficiency in CV degradation, they
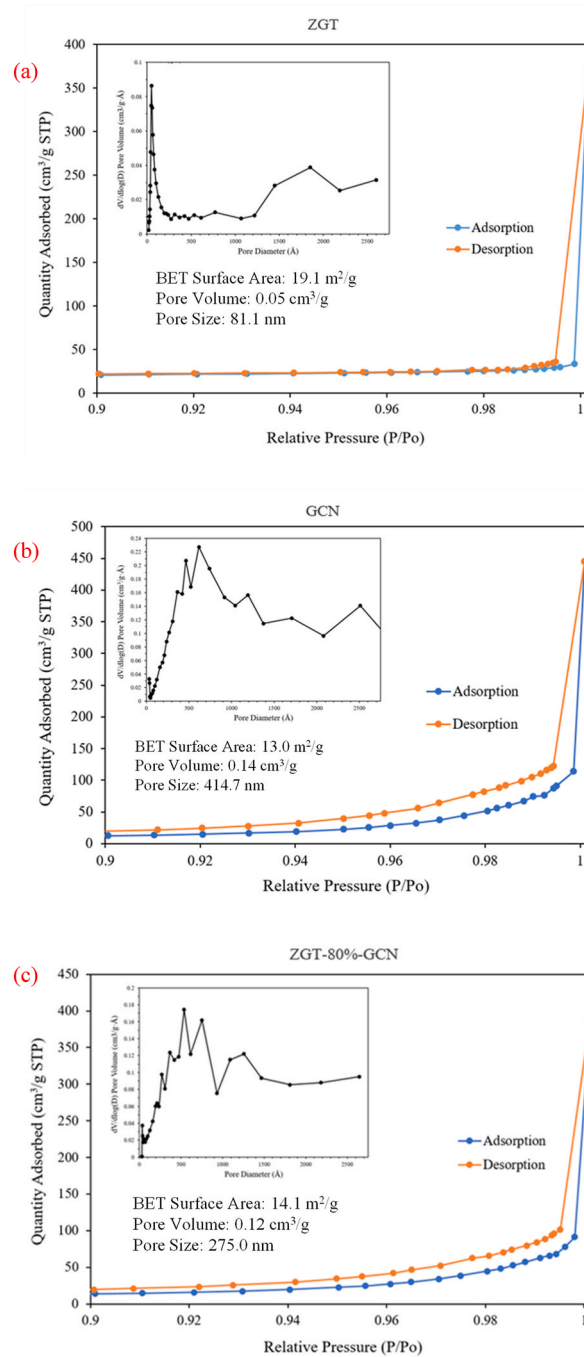
Fig. 6. N_2 adsorption–desorption isotherms and pore size distribution of (a) ZGT, (b) GCN, and (c) ZGT-80%GCN.

Table 1
Physical and chemical properties of as-prepared samples.

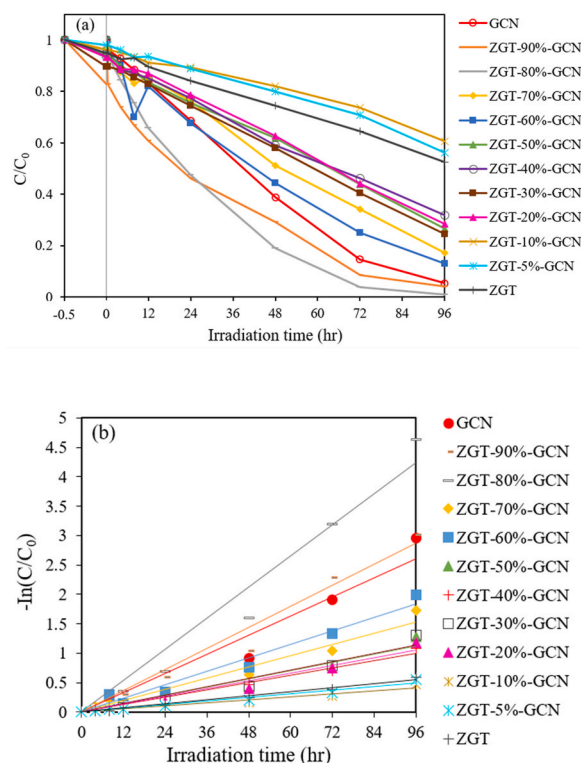| Samples	S_{BET} (m^2g^{-1})	Pore volume (cm^3g^{-1})	Pore diameter (nm)	Band gap (eV)
ZGT	19.1	0.05	81.1	3.3
ZGT-80%GCN	14.1	0.12	275.0	2.7
GCN	13.0	0.14	414.7	2.6

Fig. 7. (a) Photodegradation of CV dye as a function of irradiation time over ZGT/GCN photocatalysts; (b) Photodegradation kinetics of CV dye over ZGT/GCN photocatalysts.

Table 2
Kinetic parameters (rate constants and linear regression coefficients R^2) for photo-catalytic degradation of CV at various ZGT/GCN samples.

| Sample	k (h^{-1})	R^2
GCN	0.0272	0.9684
ZGT-90%GCN	0.0299	0.9867
ZGT-80%GCN	0.0442	0.9821
ZGT-70%GCN	0.0159	0.9787
ZGT-60%GCN	0.0192	0.9855
ZGT-50%GCN	0.0117	0.9792
ZGT-40%GCN	0.0105	0.9927
ZGT-30%GCN	0.0119	0.9744
ZGT-20%GCN	0.0110	0.9766
ZGT-10%GCN	0.0042	0.9767
ZGT-5%GCN	0.0051	0.9811
ZGT	0.0057	0.9851

required larger dosages of photocatalysts and higher light intensity compared to those employed in this work. It is essential to consider both treatment effectiveness and costs in assessing water treatment technologies for real-world applications. Many previous studies utilized high-wattage (hundreds of watts) light sources, whereas our work employed low-wattage light sources (15 W), which is favorable for low-cost treatment processes. Furthermore, using a fluorescent lamp with low light intensity in this work demonstrates that the new ZGT/GCN composites retain their photocatalytic efficiency even under weak visible light sources. The photocatalytic activity is closely linked to the photon flux, and a higher photon flux can accelerate the photocatalytic process. The slower degradation rate of CV observed in our GCN sample might be attributed to the use of a low-wattage lamp (15 W) and relatively lower light intensity during the experiment.

The photocatalytic activity of the ZGT, GCN, and ZGT-80%GCN composite in the reduction of CO_2 was determined in a closed CO_2 reactor under UV irradiation (Fig. 8). Blank experiments were carried out without the photocatalyst or CO_2, confirming that the reduction products only arise from the existence of the catalyst, CO_2 and irradiation. CH_4 was found to be the major product of CO_2 reduction using the studied photocatalysts, in addition to smaller amounts of larger hydrocarbon products (Fig. 8a-c). Increasing the irradiation time of the photocatalytic reaction increased the concentration of the CH_4 product. Under 72 h of irradiation, the yield of

Table 3

Comparison of photocatalytic activity of present work with other graphitic carbon nitride composites for crystal violet dye degradation.

Composite photocatalyst	g-C₃N₄ (wt %)	Visible lamp	Catalyst dosage (gL⁻¹)	Photocatalytic activity	Reference photocatalyst/ Enhancement factor	Reference
$Bi_{12}SiO_{20}$/g-C_3N_4	5	150 W	0.1	99 % decomposition in 48 h	g-C_3N_4: 2 $Bi_{12}SiO_{20}$: 15	[7]
Ag_3VO_4/g-C_3N_4	40	500 W	1.0	75 % decomposition in 2.5h	g-C_3N_4: 11.5 Ag_3VO_4: 6.6	[38]
$CaTiO_3$/g-C_3N_4	33.3	300 W	0.4	99.76 % decomposition in 3h	g-C_3N_4: 2.5 $CaTiO_3$: 1.5	[53]
$PbBiO_2I$/g-C_3N_4	25	150 W	0.1	99.5% decomposition in 12h	g-C_3N_4: 13.7 $PbBiO_2I$: 9.1	[54]
ZnO/g-C_3N_4	20	solar light	1.0	97 % decomposition in 3h	g-C_3N_4: 1.4 ZnO: 1.4	[55]
$CaCO_3$/g-C_3N_4	3		1.0	76 % decomposition in 3h	g-C_3N_4: 3.52	[56]
GA/g-C_3N_4	30	300 W	0.2	44.5 % decomposition in 3h		[57]
$BiOCl/BiOBr/C_3N_4$	30	15 W	0.5	99 % decomposition in 48 h	g-C_3N_4: 2.15 $BiOCl/BiOBr$: 1.65	[58]
$ZnGa_{1.01}Te_{2.13}$/g-C_3N_4	80	15 W	0.1	96 % decomposition in 72 h	g-C_3N_4: 1.63 $ZnGa_{1.01}Te_{2.13}$: 7.75	This study
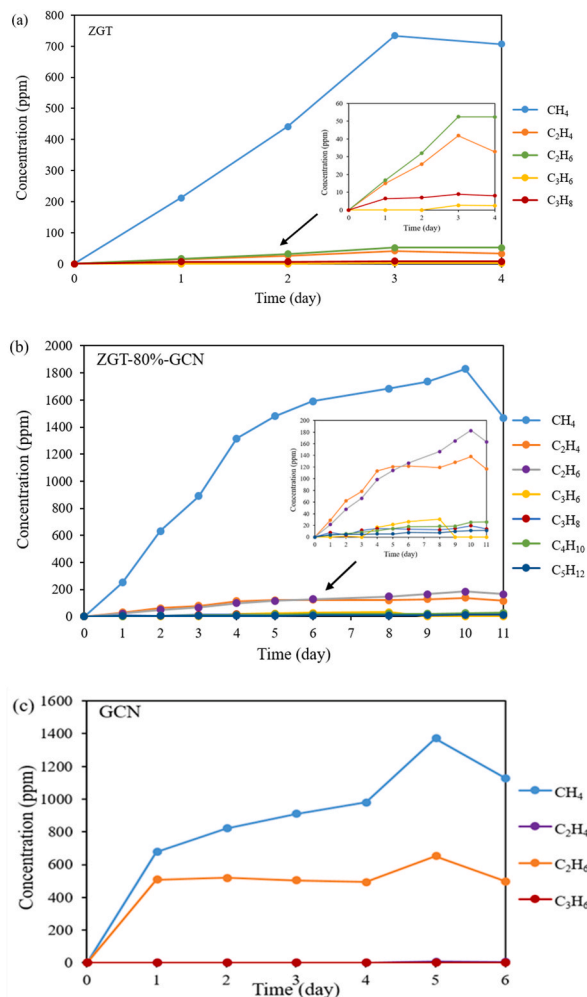
Fig. 8. Photocatalytic reduction of CO_2 as a function of irradiation time over (a) ZGT, (b) ZGT-80%GCN, and (c) GCN.

CH_4 over ZGT, GCN, and ZGT-80%GCN photocatalysts reached 0.834, 0.935, and 1.013 μmol/g, respectively, which attests for the high CO_2 conversion efficiency of the ZGT/GCN composite.

The durability of the ZGT-80%GCN composite was investigated in successive photocatalytic degradation cycles of the CV dye. After each run, the photocatalyst was collected by centrifugation and reused subsequently. Fig. 9 shows that the sample preserved its high photocatalytic activity for 5 consecutive runs. The recycling experiments demonstrate the stability and reusability of the prepared ZGT-80%GCN composite for durable photocatalytic applications without risk of photocorrosion.

The efficiency of photocatalytic activity can be assessed using photoluminescence (PL) emission spectra. An efficient photocatalyst possesses low emission intensity, indicative of a lower recombination rate of the photogenerated electrons and holes that are responsible for photocatalytic activities [37,52]. The PL spectra of GCN, ZGT and ZGT-80%GCN were measured and depicted in Fig. 10. A strong emission peak at ~458 nm is observed in the pure GCN sample, corresponding to the bandgap carrier recombination [42]. When ZGT was added, a significant decrease in the PL emission intensity was observed in the composite material, indicating the effective separation of the photoinduced charge carriers in the GCN-ZGT heterojunction. The lower relative PL intensity of the ZGT-80%GCN composite reflects a lower electron-hole recombination rate, which increases the photocatalytic activity and demonstrates the importance of the prepared heterojunction in the catalytic process. The ZGT catalyst exhibits the lowest PL intensity, but it has a band gap of around 3.3 eV, requiring UV light for activation. On the other hand, the ZGT-80%GCN composite possesses a band gap of approximately 2.7 eV, indicating good absorption of visible light and lower PL intensity compared to GCN alone. As a result, under visible light irradiation, the photocatalytic activity of ZGT-80%GCN surpasses that of both pristine ZGT and GCN.

The transient photocurrent response was evaluated through multiple on-off cycles of intermittent irradiation. The photocurrent-time (I-t) curves depicted in Fig. S4 clearly indicate notable spikes in photocurrent responses for all the tested working electrodes once pulse Xe lamp irradiation is initiated. The rapid rise in photocurrent response, observed with off-on light switches, is attributed to the efficient separation and transportation of photoinduced electrons on the surfaces of the working electrodes. The higher photocurrent density observed in the ZGT-80%GCN composite compared to pristine GCN and ZGT indicates a superior separation efficiency of photogenerated charge carriers in the obtained composites. The electrochemical impedance spectra (EIS) of the samples were recorded (Fig. S5). The arc radius of the EIS curve indicates the interface layer impedance at the electrode surface. A smaller arc radius signifies a more efficient charge transfer process [59]. The ZGT-80%GCN had a smaller arc as compared with pristine GCN and ZGT, reflecting faster migration of charge carriers in the ZGT/GCN composites.

3.3. Pathways of CV photodegradation and CO_2 photoreduction

The contributions of the main active species (h^+, $^\bullet O_2^-$, $^\bullet OH$ and $^1O_2$) in the photodegradation of the CV dye were determined using scavengers (Ammonium oxalate (AO), benzoquinone (BQ), isopropanol (IPA) and sodium azide (SA), respectively) [60]. The visible-light driven degradation of the CV dye with ZGT-80%GCN catalyst was tested in the absence and presence of the four scavengers (Fig. 11a). The inhibition effects of IPA and BQ were higher than those of AO and SA, implying that $^\bullet OH$ and $^\bullet O_2^-$ radicals were the dominant oxidative species in the degradation of CV with secondary roles for h^+ and $^1O_2$. The reactive radicals in this process were further detected using ESR spin-trap technique with DMPO (Fig. 11b-c). Irradiation of ZGT-80%GCN with visible light led to the generation of the four characteristic peaks of DMPO-•OH (1:2:2:1 quartet modes) as well as those of DMPO$^{+\bullet}$ (1:1:1 triplet modes), as can be seen in the figure. The hyperfine splitting values for DMPO-•OH and DMPO$^{+\bullet}$ were a_N = 1.492 mT and $a_{H\beta}$ = 1.484 mT and a_N = 1.463 mT, respectively. The photocatalytic process generates $^\bullet OH$ radicals which reacts with DMPO forming the detected DMPO-•OH. Nevertheless, DMPO might be oxidized prior to production of hydroxyl radicals by the holes in the valence band to form the free radical cation DMPO$^{+\bullet}$, that was also detected by ESR. To conclude, DMPO-•OH can be formed in the catalytic processes via these routes: reaction of DMPO with holes or adsorbed $^\bullet OH$ radicals on the surface or free $^\bullet OH$ in the solution or oxidation of DMPO to DMPO$^{+\bullet}$ followed by hydrolysis [61]. Characteristic signals of the DMPO–•O_2^- adduct were also observed in the reactions under visible-light irradiation. The intensity of the signals gradually increased with the prolonged reaction time. These signals confirm the
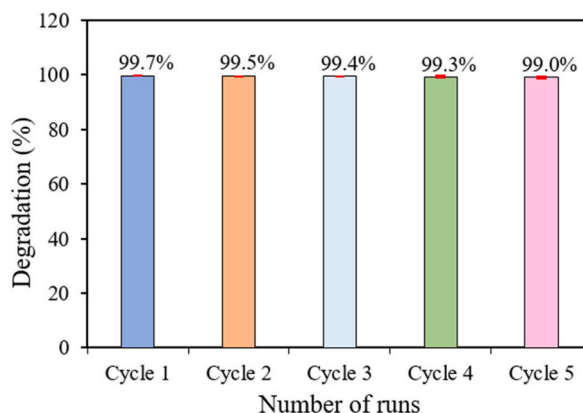

Fig. 9. Cycling runs in the photocatalytic degradation of CV in the presence of ZGT-80%GCN.
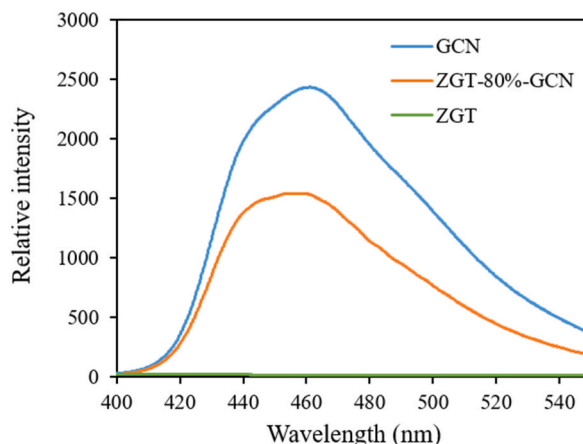
Fig. 10. PL spectra of the as-prepared ZGT, GCN, and ZGT-80%GCN.

visible-light activation of the photocatalysts and the formation of the reactive oxygen radicals in the photodegradation process, in agreement with the scavenger experiments.

A plausible mechanism for the photocatalytic activity of the ZGT/GCN heterojunction is subsequently proposed in Fig. 12. The valence band (E_{VB}) and conduction band (E_{CB}) edge potentials of ZGT and GCN were determined using ultraviolet photoelectron spectroscopy (UPS) measurements and equations (1) and (2):

$$E_{VB} = \chi - E^{\theta} + 1/2E_g \tag{1}$$

$$E_{CB} = E_{VB} - E_g \tag{2}$$

χ represents the geometric mean of electronegativities of the constituent atoms; E_g represents the band gap; and the value of E^{θ} is ~4.5 eV, which represents the energy of free electrons on the hydrogen scale. The VB positions of ZGT and GCN were determined to be 0.08 and 1.58 eV, and the CB positions were -3.22 and -1.02 eV, respectively. The irradiation of the ZGT/GCN composite caused the excitation of electrons in the valence bands (VB) of the GCN and ZGT to the corresponding conduction bands (CB), generating holes (h^+) in the VB. A type II heterojunction is formed where the photogenerated electrons tend to transfer from ZGT to GCN and the holes move to ZGT, consequently decreasing the electron-hole recombination possibility.

Computational methods enable the determination of the HOMO and LUMO energy levels of CV dye. According to the theoretical calculations conducted by Sen et al. [62], the HOMO and LUMO energy levels of CV were found to be -5.72 eV and -3.04 eV, respectively, forming a band gap of 2.68 eV, which is within the 1.8–3.2 eV range of visible excitation energy. The CV photo-degradation by ZGT/GCN heterojunction can occur via photosensitization and photocatalytic routes preceding simultaneously as shown in Fig. 12a. The generated electrons via either process react with the oxygen on the semiconductor surface producing super-oxide $^{\bullet}O_2^-$ radicals, which subsequently reacts with H^+ ions, water, and electrons to yield $^{\bullet}OH$ radicals. Similarly, H_2O or hydroxide ions can react with the photogenerated holes to yield more $^{\bullet}OH$ radicals. Singlet oxygen ($^1O_2$) species can be produced by electron transfer reaction from the $^{\bullet}O_2^-$ radicals to cation species [60]. The visible-light irradiation results in continuous cycles producing these species [63], where oxygen radicals photodegrade the CV dye after several photooxidation cycles (equation (3)).

$$CV + {}^{\bullet}OH/{}^{\bullet}O_2^- \rightarrow \text{degraded compounds} \tag{3}$$

On the other hand, the photoreduction of CO_2 could be directly initiated by the photogenerated electrons with CO_2 to form $^{\bullet}CO_2$ (Fig. 12b) [2,64–67]. The electrons could similarly be involved in reduction of water molecules forming $^{\bullet}H$ radicals, which react with carbon radicals on the surface of the photocatalyst. The latter reactions yield $^{\bullet}CH_2$ and $^{\bullet}CH_3$ intermediates radicals, and consequently CH_4 and higher hydrocarbons [64,65].

4. Conclusions

This work described the synthesis of ZGT/GCN composites for effective dye photodegradation and photocatalytic CO_2 reduction. The ZGT/GCN heterojunction showed improved photodegradation efficiency of CV dye, with optimal rate constant for ZGT-80%GCN composite that is 7.75 and 1.63 times larger than the ones achieved with ZGT and GCN photocatalysts, respectively. ZGT-80%GCN was also found to be effective in photocatalytic reduction of CO_2 achieving 1.013 μmol/g yield of CH_4 in 72 h, higher than that of ZGT and GCN by 1.21 and 1.08 times, respectively. The formation of the heterojunction between ZGT and GCN can explain the enhanced photocatalytic activities of the composite semiconductor, mainly due to the slower recombination of the photogenerated charge carriers. $^{\bullet}OH$ and $^{\bullet}O_2^-$ radicals were found to be the major active species in the CV degradation, whereas h^+ and $^1O_2$ played an assistant role in the reaction. The photocatalytic mechanisms were proposed in this study based on ESR and scavenger investigations. In sum,
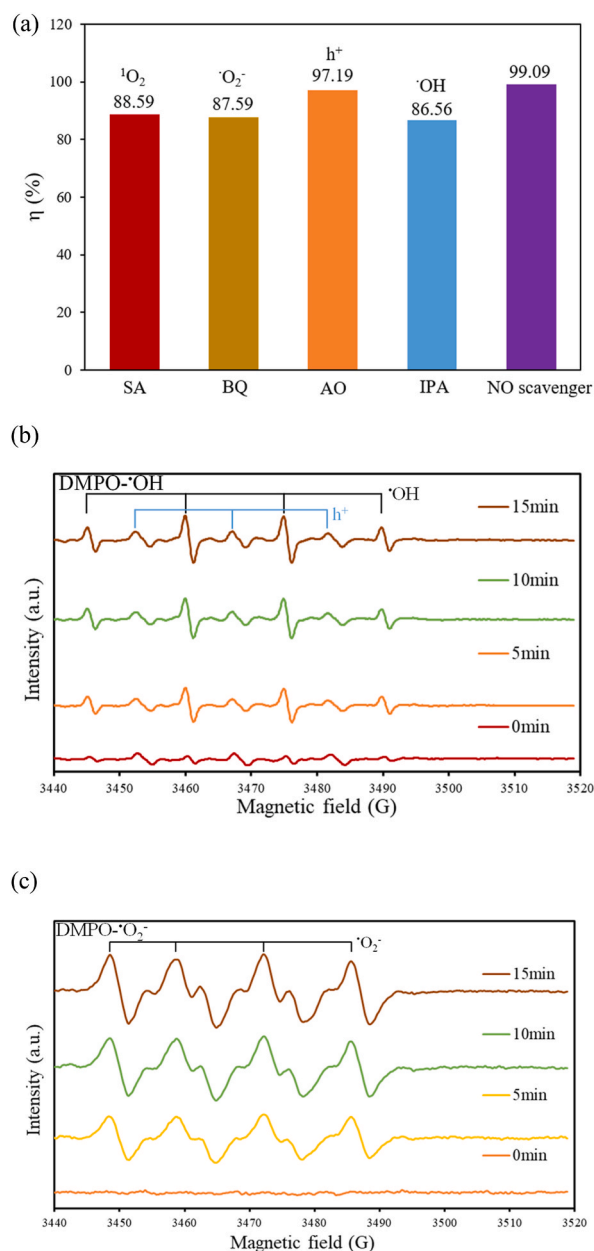
Fig. 11. (a) Trapping of active species during the photocatalytic reaction using ZGT-80%GCN, (b) and (c) ESR spectra of DMPO-•O$_2^-$ and DMPO-•OH using ZGT-80%GCN dispersion in methanol solution under visible light irradiation.

ZGT/GCN heterojunctions are efficient photocatalysts that play important roles in green technologies of CO$_2$ reduction and in the control of environmental pollution via photodegradation of organic pollutants.

Data availability statement

Data included in article/supp. material/referenced in article.

CRediT authorship contribution statement

Chiing-Chang Chen: Conceptualization, Data curation, Investigation, Methodology, Supervision. **Wen-Jin Liu:** Conceptualization, Data curation, Investigation, Methodology, Validation. **Janah Shaya:** Investigation, Methodology, Writing – review & editing. **Yu-Yun Lin:** Data curation, Investigation, Methodology. **Fu-Yu Liu:** Data curation, Investigation, Methodology. **Chao-Wei Chen:** Data
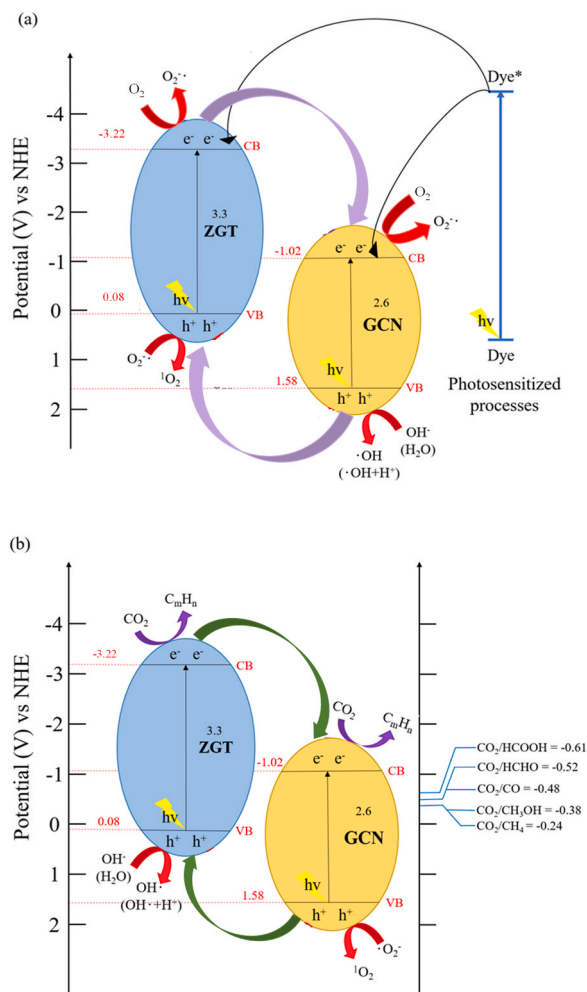
Fig. 12. The band structure diagram and possible charge separation processes of ZGT/GCN for the (a) photocatalytic degradation of CV and (b) photocatalytic reduction of CO_2.

Declaration of competing interest

The authors declare that they have no known competing financial interests or personal relationships that could have appeared to influence the work reported in this paper.

Acknowledgements

Appendix A. Supplementary data

Supplementary data to this article can be found online at https://doi.org/10.1016/j.heliyon.2023.e20879.

References

[1] T. Ma, Q. Fan, H. Tao, Z. Han, M. Jia, Y. Gao, W. Ma, Z. Sun, Heterogeneous electrochemical CO_2 reduction using nonmetallic carbon-based catalysts: current status and future challenges, Nanotechnology 28 (2017), 472001.

[2] B. Khan, F. Raziq, M. Bilal Faheem, M. Umar Farooq, S. Hussain, F. Ali, A. Ullah, A. Mavlonov, Y. Zhao, Z. Liu, H. Tian, H. Shen, X. Zu, S. Li, H. Xiao, X. Xiang, L. Qiao, Electronic and nanostructure engineering of bifunctional MoS_2 towards exceptional visible-light photocatalytic CO_2 reduction and pollutant degradation, J. Hazard Mater. 381 (2020), 120972.

[3] J. Shaya, H. Srour, I. Karamé, in: H. Srour (Ed.), Introductory Chapter: an Outline of Carbon Dioxide Chemistry, Uses and Technology, Carbon Dioxide Chemistry, Capture and Oil Recovery, InTech Open, London, UK, 2018, pp. 4–13.

[4] S.Z. Shehayeb, L. Ghannam, H. Srour, A. Kanj, J. Shaya, I. Karamé, in: B. Kharisov, O. Kharissova (Eds.), Handbook of Greener Synthesis of Nanomaterials and Compounds, Elsevier, S&T, Amsterdam, The Netherlands, 2021.

[5] X. Zhu, Y. Li, Review of two-dimensional materials for electrochemical CO_2 reduction from a theoretical perspective, Comput. Mol. Sci. 9 (2019) e1416.

[6] F. Raziq, Y. Qu, M. Humayun, A. Zada, H. Yu, L. Jing, Synthesis of SnO_2/B-P codoped $g-C_3N_4$ nanocomposites as efficient cocatalyst-free visible-light photocatalysts for CO_2 conversion and pollutant degradation, Appl. Catal. B Environ. 201 (2017) 486–494.

[7] C.-C. Chen, T.-T. Chen, J. Shaya, C.-L. Wu, C.-S. Lu, $Bi_{12}SiO_{20}/g-C_3N_4$ heterojunctions: synthesis, characterization, photocatalytic activity for organic pollutant degradation, and mechanism, J. Taiwan Inst. Chem. Eng. 123 (2021) 228–244.

[8] E. Bayram, E. Ayranci, Investigation of changes in properties of activated carbon cloth upon polarization and of electrosorption of the dye basic blue-7, Carbon 48 (2010) 1718–1730.

[9] D. Wang, Y. Li, B. Yu, H. Li, W. Jiang, X. Deng, Y. Wen, C. Liu, G. Che, Improved visible-light driven photocatalysis by loading Au onto C_3N_4 nanorods for degradation of RhB and reduction of CO_2, Adv. Powder Technol. 32 (2021) 1653–1662.

[10] H. Wang, Q. Zhang, J.J. Li, J.Y. Zhang, Y. Liu, M. Zhou, N. Zhang, Y.Z. Fang, Q. Ke, The covalent Coordination-driven $Bi_2S_3@NH_2$-MIL-125(Ti)-SH heterojunction with boosting photocatalytic CO_2 reduction and dye degradation performance, J. Colloid Interface Sci. 606 (2022) 1745–1757.

[11] C.S. Lu, H.Y. Tsai, J. Shaya, V.B. Golovko, S.Y. Wang, W.J. Liu, C.C. Chen, Degradation of sulfamethoxazole in water by $AgNbO_3$ photocatalyst mediated by persulfate, RSC Adv. 12 (2022) 29709–29718.

[12] A.K. Singh, J.H. Montoya, J.M. Gregoire, K.A. Persson, Robust and synthesizable photocatalysts for CO_2 reduction: a data-driven materials discovery, Nat. Commun. 10 (2019) 443.

[13] I.S. Yahia, M. Fadel, G.B. Sakr, S.S. Shenouda, Memory switching of $ZnGa_2Se_4$ thin films as a new material for phase change memories (PCMs), J. Alloys Compd. 507 (2010) 551–556.

[14] S. Chandra, A. Sinha, V. Kumar, Electronic and elastic properties of $A^{II}B_2^{III}C_4^{VI}$ defect-chalcopyrite semiconductors, Int. J. Mod. Phys. B 33 (2019), 1950340.

[15] G.B. Sakr, S.S. Fouad, I.S. Yahia, D.M. Abdel Basset, Memory switching of $ZnGa_2Te_4$ thin films, J. Mater. Sci. 48 (2012) 1134–1140.

[16] S.S. Fouad, G.B. Sakr, I.S. Yahia, D.M.A. Basset, Structural characterization and novel optical properties of defect chalcopyrite $ZnGa_2Te_4$ thin films, Mater. Res. Bull. 46 (2011) 2141–2146.

[17] D. Errandonea, R.S. Kumar, O. Gomis, F.J. Manjón, V.V. Ursaki, I.M. Tiginyanu, X-ray diffraction study on pressure-induced phase transformations and the equation of state of $ZnGa_2Te_4$, J. Appl. Phys. 114 (2013), 233507.

[18] F. Deng, X. Lu, L. Zhao, Y. Luo, X. Pei, X. Luo, S. Luo, Facile low-temperature co-precipitation method to synthesize hierarchical network-like $g-C_3N_4/SnIn_4S_8$ with superior photocatalytic performance, J. Mater. Sci. 51 (2016) 6998–7007.

[19] J. Chen, S. Fang, Q. Shen, J. Fan, Q. Li, K. Lv, Recent advances of doping and surface modifying carbon nitride with characterization techniques, Catalysts 12 (2022) 962.

[20] Z. Qi, J. Chen, W. Zhou, Y. Li, X. Li, S. Zhang, J. Fan, K. Lv, Synergistic effects of holey nanosheet and sulfur-doping on the photocatalytic activity of carbon nitride towards NO removal, Chemosphere 316 (2023), 137813.

[21] J. Jiang, X. Wang, Q. Xu, Z. Mei, L. Duan, H. Guo, Understanding dual-vacancy heterojunction for boosting photocatalytic CO_2 reduction with highly selective conversion to CH_4, Appl. Catal. B Environ. 316 (2022), 121679.

[22] W.J. Ong, L.L. Tan, Y.H. Ng, S.T. Yong, S.P. Chai, Graphitic carbon nitride $(g-C_3N_4)$-based photocatalysts for artificial photosynthesis and environmental remediation: are we a step closer to achieving sustainability? Chem. Rev. 116 (2016) 7159–7329.

[23] K. Li, W. Zhou, X. Li, Q. Li, S.A.C. Carabineiro, S. Zhang, J. Fan, K. Lv, Synergistic effect of cyano defects and $CaCO_3$ in graphitic carbon nitride nanosheets for efficient visible-light-driven photocatalytic NO removal, J. Hazard Mater. 442 (2023), 130040.

[24] W. Chen, T.-Y. Liu, T. Huang, X.-H. Liu, J.-W. Zhu, G.-R. Duan, X.-J. Yang, One-pot hydrothermal route to synthesize the $ZnIn_2S_4/g-C_3N_4$ composites with enhanced photocatalytic activity, J. Mater. Sci. 50 (2015) 8142–8152.

[25] J. Wen, J. Xie, X. Chen, X. Li, A review on $g-C_3N_4$-based photocatalysts, Appl. Surf. Sci. 391 (2017) 72–123.

[26] J. Chen, N. Kang, J. Fan, C. Lu, K. Lv, Carbon nitride for photocatalytic water splitting to produce hydrogen and hydrogen peroxide, Mater, Today Chem 26 (2022), 101028.

[27] X. Wang, J. Jiang, Q. Xu, L. Duan, H. Guo, Understanding inclusive quantum dots hollow CN@CIZS heterojunction for enhanced photocatalytic CO_2 reduction, Appl. Surf. Sci. 604 (2022), 154601.

[28] G. Murali, S.V. Prabhakar Vattikuti, Y.K. Kshetri, H. Lee, J.K.R. Modigunta, C. Seshendra Reddy, S. Park, S. Lee, B. Poornaprakash, H. Lee, Y.H. Park, J. Lee, S. Y. Park I, Near-infrared-activated Z-scheme $NaYF_4$:Yb/Tm@Ag_3PO_4/Ag@$g-C_3N_4$ photocatalyst for enhanced H_2 evolution under simulated solar light irradiation, Chem. Eng. J. 421 (2021), 129687.

[29] H. Hou, G. Shao, W. Yang, Recent advances in $g-C_3N_4$-based photocatalysts incorporated by MXenes and their derivatives, J. Mater. Chem. A 9 (2021) 13722–13745.

[30] Y. Zhao, H. Shi, D. Yang, J. Fan, X. Hu, E. Liu, Fabrication of a $Sb_2MoO_6/g-C_3N_4$ photocatalyst for enhanced RhB degradation and H_2 generation, J. Phys. Chem. C 124 (2020) 13771–13778.

[31] W. Zhang, C. Xu, E. Liu, J. Fan, X. Hu, Facile strategy to construction Z-scheme $ZnCo_2O_4/g-C_3N_4$ photocatalyst with efficient H_2 evolution activity, Appl. Surf. Sci. 515 (2020), 146039.

[32] H. Abbasi_Asl, Z. Moradi, M. Ghaedi, M.M. Sabzehmeidani, Degradation of Orange G and Trypan blue using $Ag_2C_2O_4$/Ag/$g-C_3N_4$ composites as efficient photocatalyst under solar irradiation, J. Photochem. Photobiol. A-Chem. 401 (2020), 112755.

[33] C. Zhao, Y. Chen, C. Li, Q. Zhang, P. Chen, K. Shi, Y. Wu, Y. He, One step and fast preparation of $VO_x/g-C_3N_4$ photocatalyst via microwave heating for effective degradation of RhB under visible light, J. Phys. Chem. Solids 136 (2020), 109122.

[34] Z. Zhang, Z. Pan, Y. Guo, P.K. Wong, X. Zhou, R. Bai, In-situ growth of all-solid Z-scheme heterojunction photocatalyst of $Bi_7O_9I_3/g-C_3N_4$ and high efficient degradation of antibiotic under visible light, Appl. Catal. B Environ. 261 (2020), 118212.

[35] W. Chen, T. Huang, Y.X. Hua, T.Y. Liu, X.H. Liu, S.M. Chen, Hierarchical $CdIn_2S_4$ microspheres wrapped by mesoporous $g-C_3N_4$ ultrathin nanosheets with enhanced visible light driven photocatalytic reduction activity, J. Hazard Mater. 320 (2016) 529–538.

[36] S.-Z. Wu, K. Li, W.-D. Zhang, On the heterostructured photocatalysts $Ag_3VO_4/g-C_3N_4$ with enhanced visible light photocatalytic activity, Appl. Surf. Sci. 324 (2015) 324–331.

[37] K. Xiao, H. Huang, N. Tian, Y. Zhang, Mixed-calcination synthesis of $Bi_2MoO_6/g-C_3N_4$ heterojunction with enhanced visible-light-responsive photoreactivity for RhB degradation and photocurrent generation, Mater. Res. Bull. 83 (2016) 172–178.

[38] S. Wang, D. Li, C. Sun, S. Yang, Y. Guan, H. He, Synthesis and characterization of $g-C_3N_4/Ag_3VO_4$ composites with significantly enhanced visible-light photocatalytic activity for triphenylmethane dye degradation, Appl. Catal. B Environ. 144 (2014) 885–892.

[39] C.C. Chen, H.J. Fan, J. Shaya, Y.K. Chang, V.B. Golovko, O. Toulemonde, C.H. Huang, Y.X. Song, C.S. Lu, Accelerated $ZnMoO_4$ photocatalytic degradation of pirimicarb under UV light mediated by peroxymonosulfate, Appl. Organomet. Chem. 33 (2019) e5113.

[40] V. Thakur, S.M. Shivaprasad, Electronic structure of GaN nanowall network analysed by XPS, Appl. Surf. Sci. 327 (2015) 389–393.

[41] M. Amin Baghchesara, M. Cheraghizade, R. Yousefi, Growth and characterization of ZnTe nanowires grown in a large scale by a CVD method, Mater. Lett. 162 (2016) 195–198.

[42] D. Jiang, J. Li, C. Xing, Z. Zhang, S. Meng, M. Chen, Two-dimensional CaIn$_2$S$_4$/g-C$_3$N$_4$ heterojunction nanocomposite with enhanced visible-light photocatalytic activities: interfacial engineering and mechanism insight, ACS Appl. Mater. Interfaces 7 (2015) 19234–19242.

[43] H. Li, J. Liu, W. Hou, N. Du, R. Zhang, X. Tao, Synthesis and characterization of g-C$_3$N$_4$/Bi$_2$MoO$_6$ heterojunctions with enhanced visible light photocatalytic activity, Appl. Catal. B Environ. 160–161 (2014) 89–97.

[44] W. Hu, J. Yu, X. Jiang, X. Liu, R. Jin, Y. Lu, L. Zhao, Y. Wu, Y. He, Enhanced photocatalytic activity of g-C$_3$N$_4$ via modification of NiMoO$_4$ nanorods, Colloid Surf. A-Physicochem. Eng. Asp. 514 (2017) 98–106.

[45] L. Zhao, L. Zhang, H. Lin, Q. Nong, M. Cui, Y. Wu, Y. He, Fabrication and characterization of hollow CdMoO$_4$ coupled g-C$_3$N$_4$ heterojunction with enhanced photocatalytic activity, J. Hazard Mater. 299 (2015) 333–342.

[46] M. Ou, Q. Zhong, S. Zhang, L. Yu, Ultrasound assisted synthesis of heterogeneous g-C$_3$N$_4$/BiVO$_4$ composites and their visible-light-induced photocatalytic oxidation of NO in gas phase, J. Alloys Compd. 626 (2015) 401–409.

[47] L. Wang, X. Li, W. Teng, Q. Zhao, Y. Shi, R. Yue, Y. Chen, Efficient photocatalytic reduction of aqueous Cr(VI) over flower-like SnIn$_4$S$_8$ microspheres under visible light illumination, J. Hazard Mater. 244–245 (2013) 681–688.

[48] M. Ismael, Facile synthesis of NiO-loaded g-C$_3$N$_4$ heterojunction photocatalyst for efficient photocatalytic degradation of 4-nitrophenol under visible light irradiation, J. Photochem. Photobiol. A-Chem. 439 (2023), 114576.

[49] F. Guo, W. Shi, X. Lin, G. Che, Hydrothermal synthesis of graphitic carbon nitride–BiVO$_4$ composites with enhanced visible light photocatalytic activities and the mechanism study, J. Phys. Chem. Solids 75 (2014) 1217–1222.

[50] X. Lu, Y. Wang, X. Zhang, G. Xu, D. Wang, J. Lv, Z. Zheng, Y. Wu, NiS and MoS$_2$ nanosheet co-modified graphitic C$_3$N$_4$ ternary heterostructure for high efficient visible light photodegradation of antibiotic, J. Hazard Mater. 341 (2018) 10–19.

[51] D. Wu, J. Li, J. Guan, C. Liu, X. Zhao, Z. Zhu, C. Ma, P. Huo, C. Li, Y. Yan, Improved photoelectric performance via fabricated heterojunction g-C$_3$N$_4$/TiO$_2$/HNTs loaded photocatalysts for photodegradation of ciprofloxacin, J. Ind. Eng. Chem. 64 (2018) 206–218.

[52] H. Tsai, J. Shaya, S. Tesana, V.B. Golovko, S.-Y. Wang, Y.-Y. Liao, C.-S. Lu, C.-C. Chen, Visible-light driven photocatalytic degradation of pirimicarb by Pt-doped AgInS$_2$ nanoparticles, Catalysts 10 (2020) 857.

[53] X. Chen, X. He, X. Yang, Z. Wu, Y. Li, Construction of novel 2D/1D g-C$_3$N$_4$/CaTiO$_3$ heterojunction with face-to-face contact for boosting photodegradation of triphenylmethane dyes under simulated sunlight, J. Taiwan Inst. Chem. Eng. 107 (2020) 98–109.

[54] L.-W. Chen, H.-L. Chen, C.-S. Lu, S.-T. Huang, T.-W. Yeh, C.-C. Chen, Preparation of perovskite-like PbBiO$_2$I/g-C$_3$N$_4$ exhibiting visible-light-driven activity, Catal. Today 375 (2021) 472–483.

[55] R. Manimozhi, M. Mathankumar, A.P.G. Prakash, Synthesis of g-C$_3$N$_4$/ZnO heterostructure photocatalyst for enhanced visible degradation of organic dye, Optik 229 (2021), 165548.

[56] P. Lu, X. Hu, Y. Li, Y. Peng, M. Zhang, X. Jiang, Y. He, M. Fu, F. Dong, Z. Zhang, Novel CaCO$_3$/g-C$_3$N$_4$ composites with enhanced charge separation and photocatalytic activity, J. Saudi Chem. Soc. 23 (2019) 1109–1118.

[57] J.-Y. Zhang, S.-H. Zhang, J. Li, X.-C. Zheng, X.-X. Guan, Constructing of 3D graphene aerogel-g-C$_3$N$_4$ metal-free heterojunctions with superior purification efficiency for organic dyes, J. Mol. Liq. 310 (2020) 113242.

[58] Y.C. Chou, Y.Y. Lin, C.S. Lu, F.Y. Liu, J.H. Lin, F.H. Chen, C.C. Chen, W.T. Wu, Controlled hydrothermal synthesis of BiO$_x$Cl$_y$/BiO$_m$Br$_n$/g-C$_3$N$_4$ composites exhibiting visible-light photocatalytic activity, J. Environ. Manage. 297 (2021) 113256.

[59] M.M. Khan, S.A. Ansari, D. Pradhan, M.O. Ansari, D.H. Han, J. Lee, M.H. Cho, Band gap engineered TiO$_2$ nanoparticles for visible light induced photoelectrochemical and photocatalytic studies, J. Mater. Chem. A 2 (2014) 637–644.

[60] C.-C. Chen, S.-H. Chang, J. Shaya, F.-Y. Liu, Y.-Y. Lin, L.-G. Wang, H.-Y. Tsai, C.-S. Lu, Hydrothermal synthesis of BiO$_x$Br$_y$/BiO$_m$I$_n$/GO composites with visible-light photocatalytic activity, J. Taiwan Inst. Chem. Eng. 133 (2022) 104272.

[61] H.L. Chen, F.Y. Liu, X. Xiao, Y.Y. Lin, J. Hu, G.Y. Liu, B. Gao, D. Zou, C.C. Chen, Photoreduction of carbon dioxide and photodegradation of organic pollutants using alkali cobalt oxides MCoO$_2$ (M = Li or Na) as catalysts, J. Environ. Manage. 313 (2022), 114930.

[62] S. Sen, C. Das, N.N. Ghosh, N. Baildya, S. Bhattacharya, M.A. Khan, M. Sillanpaa, G. Biswas, Is degradation of dyes even possible without using photocatalysts? - a detailed comparative study, RSC Adv. 12 (2022) 34335–34345.

[63] W.W. Dunn, Y. Aikawa, A.J. Bard, Characterization of particulate titanium dioxide photocatalysts by photoelectrophoretic and electrochemical measurements, J. Am. Chem. Soc. 103 (1981) 3456–3459.

[64] F. Raziq, M. Humayun, A. Ali, T. Wang, A. Khan, Q. Fu, W. Luo, H. Zeng, Z. Zheng, B. Khan, H. Shen, X. Zu, S. Li, L. Qiao, Synthesis of S-doped porous g-C$_3$N$_4$ by using ionic liquids and subsequently coupled with Au-TiO$_2$ for exceptional cocatalyst-free visible-light catalytic activities, Appl. Catal. B Environ. 237 (2018) 1082–1090.

[65] M. Tahir, N.S. Amin, Indium-doped TiO$_2$ nanoparticles for photocatalytic CO$_2$ reduction with H$_2$O vapors to CH$_4$, Appl. Catal. B Environ. 162 (2015) 98–109.

[66] A. Ahmad Beigi, S. Fatemi, Z. Salehi, Synthesis of nanocomposite CdS/TiO$_2$ and investigation of its photocatalytic activity for CO$_2$ reduction to CO and CH$_4$ under visible light irradiation, J. CO$_2$ Util. 7 (2014) 23–29.

[67] M. Tahir, B. Tahir, N.S. Amin, Photocatalytic CO$_2$ reduction by CH$_4$ over montmorillonite modified TiO$_2$ nanocomposites in a continuous monolith photoreactor, Mater. Res. Bull. 63 (2015) 13–23.